ygen consumption at the most fundamental tissue/capillary level.

To address this issue, we inhibited iNOS/NO overproduction in a rat model of hypotensive sepsis and measured capillary oxygen transport variables. Since nitric oxide synthesis is up-regulated in the first few hours following a septic insult (1), this animal study focuses on whether iNOS/NO overproduction in the early stages of hypotensive sepsis affects capillary flow distribution, capillary hemodynamics, and local tissue oxygen consumption in skeletal muscle. Here we extend our previous work (15–18) by calculating indices for capillary oxygen supply and local tissue oxygen consumption. We hypothesized that complete inhibition of NO overproduction following the onset of a septic insult would 1) prevent the development of capillary stopped-flow and subsequent maldistribution of oxygen delivery that we and others have observed in both early and late stages of sepsis (15, 16, 19); and 2) increase oxygen consumption by preventing NO-induced mitochondrial inhibition. To test these hypotheses, we pharmacologically inhibited NO overproduction in a rat model of hypotensive sepsis and used *in vivo* microvascular imaging to obtain oxygen transport and tissue oxygen consumption data at the capillary level.

MATERIALS AND METHODS

Animals. Nonfasting adult male Sprague-Dawley rats (165–180 g) were randomized to three groups: sham laparotomy (sham, n = 5), cecal ligation and perforation (CLP, n = 5), and CLP treated with the iNOS inhibitor L-N6-(1-iminoethyl)lysine dihydrochloride (CLP+L-NIL, n = 5). Experimental protocols were approved by the University of Western Ontario Council on Animal Care.

Acute CLP Sepsis Model. An acute fecal-peritonitis model of sepsis was used with continuous intravenous infusion of sodium pentobarbital (18 $mg \cdot kg^{-1} \cdot hr^{-1}$) for general anesthesia. The cecum was exposed through a midline incision, ligated distal to the ileocecal valve, and perforated by a 0.5-cm incision. Fecal contents were expressed into the peritoneum and the incision was closed. The right carotid artery and left jugular vein were cannulated (polyethylene-10, Clay Adams, and Bio-Sil tubing, Silmed, Saint-Gobain Akron, OH) for monitoring mean arterial pressure (MAP, Digi-Med Blood Pressure Analyzer, Micro-Med, Louisville, KY) and providing fluid resuscitation (0.9% saline, 10 $mL \cdot kg^{-1} \cdot hr^{-1}$), respectively. Animals were tracheotomized and mechanically ventilated (30%:70% oxygen/nitrogen). Ventilation variables and baseline blood gases were established within the normal range at the outset and were not adjusted during the experiment: P_{O_2} 85–100 torr, P_{CO_2} 35–45 torr, and pH 7.3–7.4 (ABL Radiometer Blood Gas Analyzer, ABL500, Copenhagen, Denmark), respiratory rate 72–85 breaths/min, and tidal volume 1.6–2.2 mL (Harvard Rodent Ventilator, 683, Diversified Equipment, Lorton, VA).

EDL Skeletal Muscle Preparation. Following abdominal surgery, the hind limb extensor digitorum longus (EDL) skeletal muscle was blunt dissected and severed from the tendon. The animal was moved to the imaging stage and the EDL positioned in the optical path at *in situ* length by a suture tied to the tendon. The muscle was covered by Saran-Wrap and cover slip, which acted as an oxygen barrier, and allowed to stabilize for 30 mins. Six to eight random fields of view of microvascular beds were imaged from 3.5 to 4.5 hrs following the septic injury. Equal numbers of random arteriolar-end, mid-vessel, and venular-end capillary segments were recorded for 1–2 mins. Animal core temperature was maintained between 36.5°C and 37.2°C by external heat lamp.

Functional Microvascular Imaging: Capillary Red Blood Cell Hemodynamics, Hemoglobin Oxygen Saturation, and Geometry. The microvascular imaging system has been described previously (16, 20, 21). In brief, optical density (OD) information at 420 and 430 nm from the EDL skeletal muscle microcirculation was acquired on S-VHS video tape via two high-resolution closed-circuit video systems (video monitor, WV-5410, and video cassette recorder, AG-7300, Panasonic, Osaka, Japan). This was achieved by illuminating the EDL with a 100-W xenon light source (Diaphot 300 inverted microscope, Nikon, Yokohama, Japan, and ×20/0.4 Nikon objective) and splitting the transmitted light 70:30 (beam splitter fitted with 420- and 430-nm interference filters) between two CCD cameras (MTI CCDC72, North Reading, MA). A Silicon Graphics workstation (St-Laurent, Quebec, Canada) captured identical 30-sec video sequences from both the 420- and 430-nm video tapes and stored the data on hard disk as two sets (one for each wavelength) of 900 image files in TIFF format.

Red blood cell (RBC) hemoglobin oxygen saturations (S_{O_2}) were computed for every second at every capillary segment location based on the 430-nm/420-nm optical density ratio, as previously described (22). The optical density of each flowing RBC was computed as OD = log (Io/I), where I is intensity of transmitted light passing through the RBC and Io is the intensity of incident light on the RBC. RBC oxygen saturation was computed as $S_{O_2} = a + b \cdot OD430/OD420$, where constants a and b were determined from an *in vivo* calibration against 0 and 100% oxygen using a gas chamber inserted into the microscope stage.

Capillary geometry and RBC hemodynamics were determined from the 420-nm OD information. Flowing RBCs separated by plasma gaps generate varying OD information over time as they pass through the optical path. This variance in light intensity was used to generate a variance image, which outlined the geometry (length and diameter) of the flowing RBC column (high variance) against the tissue background (low variance) (21). Capillary RBC velocity (V; μm/sec) was computed using a frame-by-frame spatial correlation technique, and RBC lineal density (LD; RBC/mm) was determined by detecting the number of RBCs in a capillary segment in each video frame (20). The RBC supply rate (SR; RBC/sec) was calculated as the product of RBC velocity and lineal density, SR = V·LD (16).

Quantification of Capillary Oxygen Flow, Oxygen Extraction, and Oxygen Flux. Using RBC hemodynamic and oxygen saturation information, oxygen flow rates (qO_2) were calculated as the product of RBC supply rate and hemoglobin oxygen saturation, $qO_2 = SR \cdot S_{O_2} \cdot K$, where K is the oxygen-carrying capacity of a single RBC (K = 0.0362 pL oxygen/RBC at 100% S_{O_2}) (16). Capillary oxygen extraction (O_2ER) was determined from oxygen flow rates at the entrance (en) and exit (ex) of a capillary segment, $O_2ER = (qO_2[en] - qO_2[ex])/qO_2(en)$. The rate of oxygen diffusion into the surrounding tissue per unit capillary surface area (flux of oxygen per $min^{-1} \mu m^{-2}$), or capillary oxygen flux (O_2flux), was calculated from oxygen flow rates and capillary geometry, $O_2flux = (qO_2[en] - qO_2[ex])/(\pi dL)$ (1), where πdL is the capillary surface area (d, diameter; L, length). Figure 1 outlines the geometry and mathematical equations used to calculate capillary oxygen flux, and Figure 2 provides an example of the O_2flux profile obtained from a single capillary over the 30-sec sampling period.

Indices for Tissue Oxygen Consumption and Oxygen Supply. Direct measurement of oxygen consumption in the tissue surrounding the capillaries was not possible; however, a tissue oxygen consumption index (CDper·O_2flux) could be calculated from the product of perfused capillary density (CDper) and capillary oxygen flux (O_2flux). The same rationale was applied to calculate a tissue oxygen supply index (CDper·qO_2[en]) from the product of perfused capillary density (CDper) and capillary oxygen flow rate (qO_2[en]).

Functional Capillary Density. While RBC hemodynamic and S_{O_2} data were determined in single in-focus flowing capillaries, the field of view contained additional information on neighboring capillary flow behavior. To quantify this behavior, three horizontal reference lines perpendicular to muscle fibers (149 μm) were drawn on a transparent film and placed over the monitor (15, 19). During video playback, capillaries that intersected reference lines were evaluated over 30 secs. Flow behavior was categorized as continuous (cont), intermittent (int), or stopped (stop) and expressed as capillary density (CD; caps/mm). Total capillary density (CDtotal) is the sum of CDcont, CDint, and CDstop, while perfused capillary density (CDper) is the sum of CDcont and CDint.

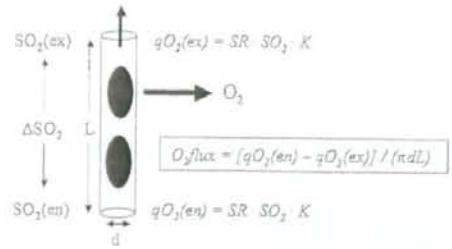

Figure 1. Schematic of O_2flux calculation. Red blood cells (RBC) flow in a capillary from bottom to top. As oxygen is off-loaded to the tissue, a red cell hemoglobin oxygen saturation gradient (ΔSO_2) develops across the length (L) of the capillary. From capillary geometry, red cell supply rate (where supply rate is the product of RBC velocity and lineal density [$SR = V{\cdot}LD$]), oxygen saturation (SO_2), and oxygen flow rates at the capillary segment entrance ($qO_2(en)$) and exit ($qO_2(ex)$), a capillary oxygen flux (O_2flux is the rate of oxygen diffusing from capillary to tissue) can be calculated. πDL, surface area of the capillary; D, capillary diameter; K, oxygen-carrying capacity of the red blood cell.

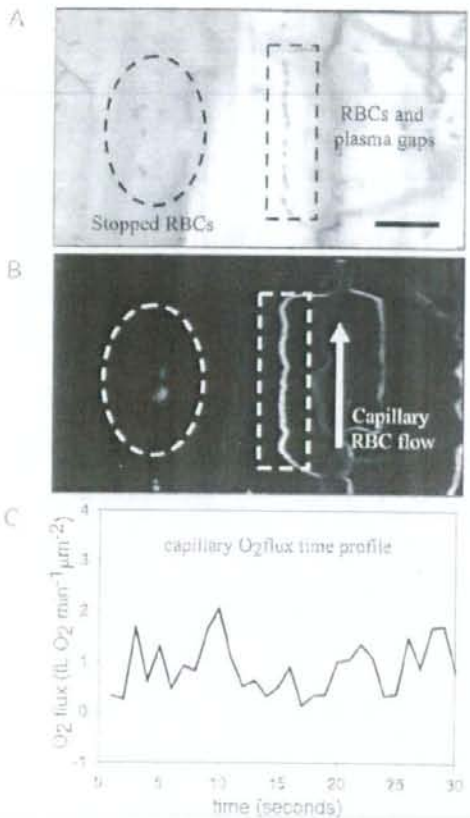

Figure 2. Example of capillary oxygen flux (O_2flux) profile. *A*, ×20 video frame of the rat hind limb extensor digitorum longus skeletal muscle microcirculation near the surface of the muscle. Dark objects are individual red blood cells (*RBCs*). *B*, 30-sec variance image depicting capillary flow (white lines against dark background). Note the capillary stopped-flow in the circled area. *C*, 30-sec O_2flux profile for the outlined capillary in *A*. Scale bar is 50 µm.

Arterial and Tissue NO_x^- Measurement. NO_x^- ($NO_2^- + NO_3^-$) was determined, as previously described (23). In brief, NO gas generated by chemical reduction of NO_x^- (0.05 M V(III) in 1 M HCl at 90°C) was detected by chemiluminescent reaction with ozone using an NO analyzer (Sievers 270b, Boulder, CO). The system was calibrated against known concentrations of NO_3^-. Arterial blood (250 µL) was collected isovolemically and deproteinized (1:1 whole blood/acetonitrile) to prevent hemoglobin interference (24). Samples were stored at −20°C and analyzed within 6 hrs. Frozen EDL tissue was homogenized in cold phosphate-buffered saline (1:15 wt/vol), filtered for 80 mins to remove tissue debris, and stored at −80°C before analysis.

Drug Dose and Delivery. To completely inhibit iNOS/NO overproduction, the specific iNOS inhibitor L-NIL (25–27) (Sigma, St. Louis, MO) was administered by venous infusion (3 mg·kg^{-1}·hr^{-1}) starting 1 hr after CLP.

Immunoblots for NOS Isoforms. To determine which NOS isoforms were up-regulated, Western blots were performed using a standard protocol as previously described (28). Briefly, frozen samples of EDL muscles were homogenized in five volumes (wt/vol) of homogenizing buffer (20 mM Tris-Cl, 1 mM EGTA, 1 mM EDTA, 1 mM DTT, 1 mM PMSF, 20 µg/mL leupeptin, and 1% triton × 100) and centrifuged (10,000 rpm for 20 mins at 4°C). The supernatant was mixed 1:1 with a sodium dodecyl sulfate glycerol buffer (125 mM Tris-HCl [pH 6.8], 20% glycerol, 4% sodium dodecyl sulfate, 2% β-mercaptoethanol, and 0.01% bromophenol blue), denatured at 95°C for 5–10 mins, resolved (25 µL/well) on a 7.5% polyacrylamide gel, and transferred to a polyvinylidene difluoride membrane. Membranes were blocked with 5% nonfat skim milk; incubated with mouse anti-neuronal NOS (nNOS) monoclonal antibody (mAb) (1:1000 in blocking buffer; BD Biosciences Transduction Laboratories, Mississauga, ON), mouse anti-endothelial NOS (eNOS) mAb (1:1000; BD Biosciences Transduction Laboratories), rabbit anti-iNOS polyclonal antibody (1:500; BD Biosciences Transduction Laboratories), or mouse anti-glyceraldehyde phosphate dehydrogenase mAb (1:10,000; Helena Biosciences, Hornby, ON) for 2 hrs; washed; and further incubated with the appropriate peroxidase-labeled anti-mouse or anti-rabbit immunoglobulin G antibody (1:1000, 1 hr at room temperature). Blots were washed and banding was visualized using an enhanced chemiluminescence kit (LUMIGLO, KPL laboratories, Gaithersburg, MA) with Kodak BIOMAX MR imaging film (Rochester, NY). Glyceraldehyde phosphate dehydrogenase was visualized using metal-enhanced DAB reagent (3,3'-diaminobenzidine; Roche Diagnostics, Laval, Quebec).

Statistical Analysis. Data are reported as median and range (25th–75th percentiles). Between-group differences in functional capillary density, oxygen transport, tissue NO_x^-, and blood gases were evaluated using non-

parametric Kruskal-Wallis one-way analysis of variance on ranks with multiple pairwise comparisons using Dunn's test. Within-group differences in blood NO_x^- and MAP over time were evaluated using nonparametric Friedman's one-way repeated measures analysis of variance on ranks with multiple pairwise comparisons against baseline using Dunnett's test. We considered $p < .05$ to be statistically significant. All statistical tests were performed using Systat, version 3.0 (Point Richmond, CA).

RESULTS

CLP Increases EDL Tissue and Blood NO_x^- Levels. Five hours after septic injury, iNOS protein expression increased in EDL skeletal muscle. There were no changes in either eNOS or nNOS protein expression (Fig. 3*A*). Corresponding with increased iNOS expression was a 68% increase ($p < .05$) in EDL tissue NO_x^- and a two-fold increase ($p < .05$) in arterial blood NO_x^- (Fig. 3, *B* and *C*, respectively). We pharmacologically targeted iNOS by constant infusion of the iNOS inhibitor L-NIL and found that both systemic NO_x^- and EDL tissue NO_x^- levels were maintained at baseline (Fig. 3, *B* and *C*). L-NIL treatment attenuated the fall in MAP observed in CLP animals but did not restore MAP to baseline (Fig. 3*D*). All animals survived 5 hrs after septic injury.

Sepsis Increases Capillary Stopped-Flow, and Inhibiting NO Overproduction in CLP Animals Increases EDL Capillary RBC Velocity. Visual assessment of capillary flow behavior in EDL skeletal muscle microvascular beds revealed that septic injury increased capillary stopped-flow 2.6-fold: CDstop was 7.7 (5.9–11.1) caps/mm in CLP vs. 2.3 (2.2–4.5) caps/mm in sham, respectively ($p < .05$, Table 1). Inhibiting iNOS/NO overproduction had no effect on capillary stopped-flow. Microvascular imaging analysis of continuous-flow capillaries revealed that RBC velocity was unchanged in CLP animals compared with sham but increased 48% when NO was inhibited in CLP animals: 105 (90.6–120) μm/sec in CLP vs. 148 (140–185) μm/sec in CLP+L-NIL ($p < .05$, Table 2). While RBC LD remained unchanged, the increase in RBC velocity resulted in a trend ($p = .12$) toward an increase in capillary RBC supply rate (SR = V·LD) in CLP+L-NIL animals. There were no differences in capillary geometry between groups.

Sepsis Increases the Capillary So_2 Gradient and Oxygen Flux, and Inhibiting NO Overproduction Increases Tissue Oxygen Consumption. Microvascular imaging analysis of RBC hemoglobin oxygen saturation (So_2) in continuous-flow capillaries revealed that sepsis increased So_2 gradients (ΔSo_2) along capillary segments in septic and iNOS/NO-inhibited septic animals (ΔSo_2 was 5.7% ± 2.0% in sham vs. 13.6% ± 4.6% in CLP and 15.8% ± 4.0% in CLP+L-NIL, $p < .05$, respectively, Table 2). We found oxygen flux (O_2flux) into the tissue increased in both CLP and CLP+L-NIL animals: O_2flux was 0.33 (0.26–0.72) fL oxygen $min^{-1}\mu m^{-2}$ in sham vs. 1.4 (1.2–1.6) fL oxygen $min^{-1}\mu m^{-2}$ in CLP and 1.5 (1.1–1.8) fL oxygen $min^{-1}\mu m^{-2}$ in CLP+LNIL, $p < .05$, respectively (Table 2).

By taking perfused capillary density into account, we were able to calculate indices for both local capillary oxygen delivery (CDper·qO_2[en]) and local tissue oxygen consumption (CDper·O_2flux). While there

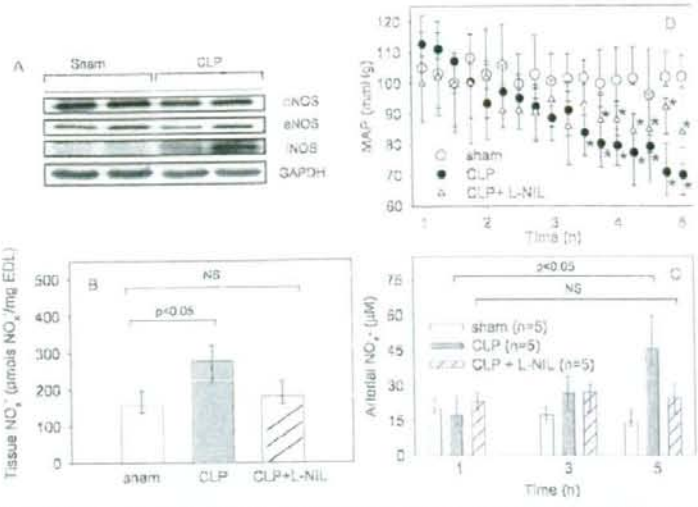

Figure 3. Sepsis-induced changes in extensor digitorum longus nitric oxide synthase (*NOS*) expression, tissue and blood NO_x^-, and mean arterial pressure (*MAP*). *A*, Western blot revealed that only inducible NOS (*iNOS*) protein expression increased by 5 hrs. Values are median and range (25th–75th percentiles). *B*, at 5 hrs, skeletal muscle tissue NO_x^- (NO_3^- + NO_2^-) was elevated, but inhibiting iNOS/NO maintained it at sham levels. *C*, similarly, arterial blood NO_x^- increased in cecal ligation and perforation (*CLP*) animals following septic injury and was maintained at baseline by treatment with L-N6-(1-iminoethyl)lysine dihydrochloride (*L-NIL*). *D*, MAP decreased following CLP, and inhibiting NO overproduction (*CLP+L-NIL*) partially restored MAP to baseline. Between-group differences in tissue NO_x^- level and within-group differences in blood NO_x^- and MAP over time were evaluated using Kruskal-Wallis one-way analysis of variance on ranks and Friedman's one-way repeated measures analysis of variance on ranks, respectively. *$p < .05$ vs. baseline. *nNOS*, neuronal NOS; *eNOS*, endothelial NOS; *GAPDH*, glyceraldehyde phosphate dehydrogenase; *NS*, not significant.

Table 1. Sepsis alters capillary flow behavior

	Sham	CLP	CLP + L-NIL	*p* Value
CDcont, caps/mm	16.2 (14.2–21.3)	16.8 (15.5–17.8)	19.1 (17.8–31.3)	NS
CDint, caps/mm	2.3 (0–3.1)	2.2 (1.3–7.5)	1.3 (0–2.9)	NS
CDstop, caps/mm	2.3 (2.2–4.5)	7.7 (6.0–11.1)*	9.5 (8.1–11.8)*	<.05
CDper, caps/mm	23.8 (20.6–26.3)	24.0 (17.2–24.2)	24.0 (19.7–32.9)	NS
ICD, Mm	43.7 (38.0–49.2)	41.6 (41.3–58.2)	41.6 (30.7–51.1)	NS
CDtotal, caps/mm	28.1 (25.0–29.0)	29.3 (28.0–31.5)	36.2 (30.7–38.8)	NS

CLP, cecal ligation and perforation; L-NIL, L-N6-(1-iminoethyl)lysine dihydrochloride; CDcont, continuous capillary density; NS, not significant; CDint, intermittent capillary density; CDstop, stopped capillary density; CDper, perfused flow capillary density; ICD, intercapillary distance; CDtotal, total V.

*$p < .05$ vs. sham. Capillary density was based on capillaries containing red blood cells. Capillary flow behavior was categorized over a 30-sec interval. CDper = CDcont + CDint, while CDtotal = CDcont + CDint + CDstop. Between-group differences were evaluated by Kruskal-Wallis one-way analysis of variance on ranks. Values are median and range (25th–75th percentiles).

Table 2. Capillary geometry, red blood cell (RBC) hemodynamics, and oxygen transport variables during septic shock

	Sham (n = 56)	CLP (n = 47)	CLP + LNIL (n = 43)	*p* Value
Geometry				
Length, μm	117 (103–118)	99 (95.6–121)	123 (113–126)	NS
Diameter, μm	5.5 (5.4–5.7)	5.6 (5.4–5.7)	5.4 (5.3–5.5)	NS
Hemodynamics				
Velocity, μm/sec	113 (109–139)	105 (90.7–120)	148 (140–185)[a]	<.05
Lineal density, RBC/mm	82.6 (70.4–104)	91.4 (85.6–104)	94.3 (75.2–106)	NS
Supply rate, RBC/sec	8.5 (5.9–9.1)	7.8 (6.8–8.2)	10.4 (8.1–16.1)	NS
Oxygen transport				
So_2(en), %	39.1 (32.2–43.4)	33.4 (30.4–46.2)	29.8 (29.0–48.1)	NS
So_2(ex), %	31.6 (29.2–33.2)	20.0 (14.9–28.8)	13.9 (11.4–21.6)[b]	<.05
ΔSo_2, %	6.3 (3.6–7.2)	14.5 (10.8–16.3)[b]	17.1 (13.1–18.1)[b]	<.05
qO_2(en), fL O_2 sec^{-1}	121 (111–169)	104 (101–198)	201 (119–226)	NS
qO_2(ex), fL O_2 sec^{-1}	109 (91.2–143)	89.6 (38.9–110)	91.9 (61.5–107)	NS
O_2ER, %	14.6 (12.9–17.0)	35.6 (29.4–41.9)	54.6 (45.5–62.9)[b]	<.05
O_2flux, fL O_2 min^{-1} μm^{-2}	0.33 (0.26–0.73)	1.4 (1.2–1.7)[b]	1.5 (1.1–1.8)[b]	<.05
CDper-qO_2(en), caps mm^{-1}· pL O_2 sec^{-1}	2.8 (1.8–4.2)	1.8 (1.8–2.0)	1.8 (1.7–2.9)	NS
CDper-O_2flux, caps mm^{-1}· fL O_2 min^{-1} μm^{-2}	4.2 (3.3–20.5)	22.5 (19.1–33.6)	45.2 (30.3–46.5)[b]	<.05

n, total number of capillaries analyzed in each group; CLP, cecal ligation and perforation; L-NIL, L-N6-(1-iminoethyl)lysine dihydrochloride; NS, not significant; So_2, oxygen saturation; en, entrance of capillary segment; ex, exit of capillary segment; ΔSo_2, RBC hemoglobin oxygen saturation gradient along a capillary segment; qO_2, oxygen flow rate; O_2ER, capillary oxygen extraction ratio; O_2flux, capillary oxygen flux; CDper, perfused capillary density.

[a]$p < .05$ vs. CLP; [b]$p < .05$ vs. sham. Values are median and range (25th–75th percentiles). Capillary length and diameter were determined from variance images (Figure 2*B*) and used to calculate capillary surface area. RBC hemodynamics and So_2 were used to calculate qO_2, O_2ER, and O_2flux. Indexes of local capillary oxygen delivery and local tissue oxygen consumption were approximated by CDper-qO_2(en) and CDper-O_2flux, respectively. Between-group differences were evaluated by Kruskal-Wallis one-way analysis of variance on ranks.

Table 3. Arterial blood gases at 5 hrs

	Sham	CLP	CLP + L-NIL	*p* Value
Pao_2, torr	92.6 (88.6–111)	109.4 (106–113)	98.6 (95.7–109)	NS
Sao_2, %	93.8 (90.0–98.4)	93.7 (92.1–95.5)	95.2 (93.5–96.6)	NS
$Paco_2$, torr	38.4 (37.2–40.0)	35.5 (33.7–37.0)	34.7 (33.0–35.9)	NS
pH	7.44 (7.42–7.45)	7.31 (7.30–7.37)[a]	7.40 (7.38–7.42)	<.05
Hb, g/dL	12.0 (11.3–12.2)	15.3 (15.1–15.9)[a]	14.3 (13.8–14.3)	<.05

CLP, cecal ligation and perforation; L-NIL, L-N6-(1-iminoethyl)lysine dihydrochloride; NS, not significant; Sao_2, arterial oxygen saturation; Hb, hemoglobin.

[a]$p < .05$ vs. sham. Normal Hb range in rat is 11.5–16 g/dL. Between-group differences were evaluated using Kruskal-Wallis one-way analysis of variance on ranks. Values are median and range (25th–75th percentiles).

was no detectable change in CDper-qO_2(en) between groups, there was a significant increase in CDper-O_2flux when nitric oxide overproduction was inhibited in septic animals ($p < .05$, Table 2), indicating that local EDL tissue oxygen consumption had increased when iNOS/NO overproduction was inhibited. This difference in oxygen consumption was reflected in changes in capillary oxygen extraction, where inhibiting iNOS/NO overproduction increased capillary oxygen extraction 43% above that of septic animals: from 35.5% (29.4–41.9) in CLP to 54.6% (45.5–62.9) in CLP+L-NIL, vs. 14.6% (12.9–16.9) in sham ($p < .05$, Table 2).

Blood Gases. Arterial Po_2, Pco_2, and So_2 were normal in all three groups at 5 hrs (Table 3). Arterial pH decreased in CLP animals: from 7.44 (7.42–7.45) in sham to 7.31 (7.30–7.37) in CLP ($p < .05$, Table 3). Inhibiting iNOS/NO overproduction prevented the fall in pH in CLP+L-NIL animals. Whole blood hemoglobin levels were elevated in CLP animals but remained within the normal rat physiologic range. Inhibiting NO overproduction in CLP+L-NIL animals maintained hemoglobin at sham level.

DISCUSSION

The key finding of this study was that inhibiting iNOS/NO overproduction during the onset of hypotensive sepsis increased skeletal muscle tissue oxygen consumption. We estimate that NO overproduction was able to reduce local EDL skeletal muscle oxygen consumption approximately 50%. This finding is in agreement with *in vitro* studies showing that NO donors inhibit mitochondrial respiration and reduce tissue oxygen consumption (3–5). Moreover, iNOS/NO overproduction modulates local *in vivo* oxygen consumption at a time when microvascular dysfunction and increased capillary stopped-flow lead to maldistribution of capillary red cell flow and increased heterogeneity of oxygen delivery. It is unknown what effect such a drop in mitochondrial respiration has on metabolic flux, energetic status, or cellular function, and this requires further investigation. However, evidence of increased capillary oxygen extraction and elevated arterial pH in iNOS/NO-inhibited septic animals is consistent with a shift toward increased aerobic metabolism. Early goal-directed therapy in septic patients, which attempted to balance oxygen delivery with oxygen demand, resulted in a similar increase in arterial pH (29).

Our animal study demonstrates that NO-mediated decrease in local skeletal muscle oxygen consumption occurs early in sepsis and can be prevented by maintaining NO production at baseline. Since Torres et al. (5) showed that NO competitively inhibits mitochondrial complex IV at low oxygen concentrations, one implication from our study is that increased oxygen demand and microvascular dysfunction establish microenvironmental Po_2 conditions that allow increased NO levels to outcompete reduced oxygen levels for binding to cytochrome *c* oxidase (complex IV), thereby reducing tissue oxygen consumption. While our study shows that the EDL tissue continues to consume oxygen and supports findings indicating that mitochondrial inhibition is reversible (2, 3), evidence of increased tissue Po_2, reduced complex I activity, and decreased adenosine triphosphate in skeletal muscle of septic patients (30, 31) suggests there is a transition at some point in the progression of sepsis from reversible to nonreversible mitochondrial

inhibition, allowing oxygen levels to increase in the tissue.

While much is known about the inflammatory and coagulation response to bacterial infection and trauma, the precise etiology of sepsis-induced multiorgan failure remains to be fully elucidated (32). In septic patients, changes in both sublingual microvascular perfusion density (33–35) and skeletal muscle mitochondrial electron transport activity (31) have been associated with sepsis severity and patient outcome. These findings implicate both microvascular dysfunction (local oxygen delivery and distribution) and mitochondrial respiration (local oxygen consumption) as critical factors in sepsis. In our animal study, we provide evidence that both local microvascular oxygen distribution and local oxygen consumption are altered during the onset of septic injury, suggesting that both factors are involved concurrently in modulating tissue metabolism and possibly muscle function. If similar microvascular dysfunction and local tissue hypoxia occurred in other organs including the liver, kidney, and heart (36, 37) at a time when iNOS was up-regulated and NO overproduced, it is possible that NO-mediated decreased mitochondrial function and reduced local oxygen consumption could contribute to alterations in organ function.

Microvascular Function, Oxygen Transport, and Nitric Oxide. Inhibiting iNOS/NO overproduction had the concurrent effects of increasing local tissue oxygen consumption while increasing capillary RBC velocity. It failed, however, to prevent capillary stopped-flow. Our finding of increased local RBC velocity was supported by Gocan et al. (38), who found that inhibiting nNOS in rat septic skeletal muscle at 24 hrs restored arteriolar responsiveness to acetylcholine and increased downstream capillary RBC velocity. It is not clear, however, how inhibiting iNOS at 5 hrs and nNOS at 24 hrs produces similar microvascular effects. The discrepancy may be related to a shift in NOS profile over time (38, 39) as both nNOS and iNOS affect arteriolar function during sepsis (28, 40). The failure of L-NIL to prevent capillary stopped-flow, however, was in contrast to our findings with the widely used iNOS inhibitor aminoguanidine, which attenuated increased stopped-flow (15). We suspect this discrepancy is because aminoguanidine has both NOS inhibition and antioxidant properties (41), whereas L-NIL does not. While reports show that NO controls capillary perfusion during hypoxia in normal animals (42) and oxidative stress (43) affects capillary density during sepsis, further research is required to fully elucidate the cause and effect relationships between NO and reactive oxygen species on capillary perfusion under pathologic conditions.

Clinical Relevance. The concept of NO inhibition as a therapy for sepsis is still debatable. Despite discontinuation of a clinical trial assessing the nonspecific NOS inhibitor 546C88 (12), this unexpected result was in contrast to the trend toward reduced mortality observed in its phase II clinical study. Thus significant differences existed between the methodologies of these two trials that resulted in a greater number of patients receiving the high dose of nonspecific NOS inhibitor in the prematurely discontinued multicenter trial. Our results in an animal model suggest that early inhibition of iNOS/NO overproduction and maintenance of NO levels at baseline could be potentially beneficial (i.e., increased local oxygen consumption in skeletal muscle) despite incomplete restoration of MAP to baseline. Increasing the dose of iNOS inhibitor to fully restore MAP may impose a detrimental effect, by increasing systemic vascular resistance and reducing cardiac output and oxygen delivery to tissues already stressed by a dysfunctional microcirculation. This raises important clinical questions: Can targeted NOS inhibition be beneficial if started early enough? To what degree should NO be inhibited to achieve a beneficial effect? The primary cause of death in the randomized trial was cardiac decompensation; however, it is unclear to what degree NO was inhibited. Further research is required to determine whether there is a window for a beneficial effect of inhibiting NO overproduction during sepsis.

Study Limitations. We obtained capillary oxygen transport and tissue oxygen consumption information at the local capillary/tissue interface and not over the entire tissue. The imaging system is limited to capillaries with RBC velocities <1000 μm/sec and lineal densities of 180 RBC/mm, which precludes measurement of a smaller number of capillaries, perhaps 10% to 15% (19) with hyperflow. Biosimulations indicate that these vessels supply large amounts of oxygen to the tissue (17); however, we were unable to assess oxygen consumption in these local areas. A second limitation was our focus on iNOS/NO exclusively. Reports indicate that eNOS is capable of regulating mitochondrial respiration under normal conditions (7, 44), although we suspect its influence to be minimal under septic conditions as iNOS is the source of NO overproduction. The possibility that neuronal NOS or its splice variant, the putative mitochondrial NOS (45), inhibits mitochondrial respiration in sepsis is intriguing and warrants further investigation. An additional study limitation is that while we found no evidence of increased MAP following L-NIL infusion, suggesting that L-NIL did not nonspecifically inhibit eNOS, treating sham animals with L-NIL may have uncovered any nonspecific NOS inhibition effects.

CONCLUSION

During the onset of hypotensive sepsis, iNOS/NO overproduction reduces tissue oxygen consumption in rat skeletal muscle. Concurrent microvascular dysfunction may facilitate this phenomenon by reducing the Po_2 in the tissue microenvironment.

ACKNOWLEDGMENTS

We acknowledge the technical assistance of Stephanie Milkovich with calibration of the spectrophotometric functional imaging, and we thank Karey Shumansky for reviewing the statistical analyses.

REFERENCES

1. Bateman RM, Sharpe MD, Ellis CG: Bench-to-bedside review: Microvascular dysfunction in sepsis—hemodynamics, oxygen transport, and nitric oxide. *Crit Care* 2003; 7:359–373
2. Davies NA, Cooper CE, Stidwill R, et al: Inhibition of mitochondrial respiration during early stage sepsis. *Adv Exp Med Biol* 2003; 530:725–736
3. Clementi E, Brown GC, Feelisch M, et al: Persistent inhibition of cell respiration by nitric oxide: Crucial role of S-nitrosylation of mitochondrial complex I and protective action of glutathione. *Proc Natl Acad Sci U S A* 1998; 95:7631–7636
4. Frost MT, Wang Q, Moncada S, et al: Hypoxia accelerates nitric oxide-dependent inhibition of mitochondrial complex I in activated macrophages. *Am J Physiol Regul Integr Comp Physiol* 2005; 288:R394–R400
5. Torres J, Darley-Usmar V, Wilson MT: Inhibition of cytochrome c oxidase in turnover by nitric oxide: Mechanism and implications for control of respiration. *Biochem J* 1995; 312: 169–173
6. Anning PB, Sair M, Winlove CP, et al: Abnormal tissue oxygenation and cardiovascular

changes in endotoxemia. *Am J Respir Crit Care Med* 1999; 159:1710–1715
7. Shen W, Hintze TH, Wolin MS: Nitric oxide: An important signaling mechanism between vascular endothelium and parenchymal cells in the regulation of oxygen consumption. *Circulation* 1995; 92:3505–3512
8. Siegemund M, van Bommel J, Schwarte LA, et al: Inducible nitric oxide synthase inhibition improves intestinal microcirculatory oxygenation and CO2 balance during endotoxemia in pigs. *Intensive Care Med* 2005; 31: 985–992
9. Avontuur JA, Tutein Nolthenius RP, van Bodegom JW, et al: Prolonged inhibition of nitric oxide synthesis in severe septic shock: A clinical study. *Crit Care Med* 1998; 26: 660–667
10. Broccard A, Hurni JM, Eckert P, et al: Tissue oxygenation and hemodynamic response to NO synthase inhibition in septic shock. *Shock* 2000; 14:35–40
11. Watson D, Grover R, Anzueto A, et al: Cardiovascular effects of the nitric oxide synthase inhibitor NG-methyl-L-arginine hydrochloride (546C88) in patients with septic shock: Results of a randomized, double-blind, placebo-controlled multicenter study (study no. 144-002). *Crit Care Med* 2004; 32:13–20
12. Lopez A, Lorente JA, Steingrub J, et al: Multiple-center, randomized, placebo-controlled, double-blind study of the nitric oxide synthase inhibitor 546C88: Effect on survival in patients with septic shock. *Crit Care Med* 2004; 32:21–30
13. Grover R, Zaccardelli D, Colice G, et al: An open-label dose escalation study of the nitric oxide synthase inhibitor, N(G)-methyl-L-arginine hydrochloride (546C88), in patients with septic shock. Glaxo Wellcome International Septic Shock Study Group. *Crit Care Med* 1999; 27:913–922
14. Statman R, Cheng W, Cunningham JN, et al: Nitric oxide inhibition in the treatment of the sepsis syndrome is detrimental to tissue oxygenation. *J Surg Res* 1994; 57:93–98
15. Bateman RM, Jagger JE, Sharpe MD, et al: Erythrocyte deformability is a nitric oxide-mediated factor in decreased capillary density during sepsis. *Am J Physiol Heart Circ Physiol* 2001; 280:H2848–2856
16. Ellis CG, Bateman RM, Sharpe MD, et al: Effect of a maldistribution of microvascular blood flow on capillary O(2) extraction in sepsis. *Am J Physiol Heart Circ Physiol* 2002; 282:H156–H164
17. Goldman D, Bateman RM, Ellis CG: Effect of sepsis on skeletal muscle oxygen consumption and tissue oxygenation: Interpreting capillary oxygen transport data using a mathematical model. *Am J Physiol Heart Circ Physiol* 2004; 287:H2535–H2544
18. Goldman D, Bateman RM, Ellis CG: Effect of decreased oxygen supply on skeletal muscle oxygenation and oxygen consumption during sepsis: Role of heterogeneous capillary spacing and blood flow. *Am J Physiol Heart Circ Physiol* 2006; 290:H2277–H2285
19. Lam C, Tyml K, Martin C, et al: Microvascular perfusion is impaired in a rat model of normotensive sepsis. *J Clin Invest* 1994; 94: 2077–2083
20. Japee SA, Pittman RN, Ellis CG: A new video image analysis system to study red blood cell dynamics and oxygenation in capillary networks. *Microcirculation* 2005; 12:489–506
21. Japee SA, Ellis CG, Pittman RN: Flow visualization tools for image analysis of capillary networks. *Microcirculation* 2004; 11:39–54
22. Ellsworth ML, Pittman RN, Ellis CG: Measurement of hemoglobin oxygen saturation in capillaries. *Am J Physiol* 1987; 252: H1031–H1040
23. Bateman RM, Ellis CG, Freeman DJ: Optimization of nitric oxide chemiluminescence operating conditions for measurement of plasma nitrite and nitrate. *Clin Chem* 2002; 48:570–573
24. Bateman RM, Ellis CG, Sharpe MD, et al: Effect of hemolyzed plasma on the batch measurement of nitrate by nitric oxide chemiluminescence. *Clin Chem* 2001; 47: 1847–1851
25. Chlopicki S, Olszanecki R, Jakubowski A, et al: L-N6-(1-iminoethyl)-lysine (L-NIL) but not S-methylisothiourea sulphate (SMT) displays selectivity towards NOS-2. *Pol J Pharmacol* 1999; 51:443–447
26. Hansel TT, Kharitonov SA, Donnelly LE, et al: A selective inhibitor of inducible nitric oxide synthase inhibits exhaled breath nitric oxide in healthy volunteers and asthmatics. *FASEB J* 2003; 17:1298–1300
27. Moore WM, Webber RK, Jerome GM, et al: L-N6-(1-iminoethyl)lysine: A selective inhibitor of inducible nitric oxide synthase. *J Med Chem* 1994; 37:3886–3888
28. McKinnon RL, Lidington D, Bolon M, et al: Reduced arteriolar conducted vasoconstriction in septic mouse cremaster muscle is mediated by nNOS-derived NO. *Cardiovasc Res* 2005; 69:236–244
29. Rivers E, Nguyen B, Havstad S, et al: Early goal-directed therapy in the treatment of severe sepsis and septic shock. *N Engl J Med* 2001; 345:1368–1377
30. Boekstegers P, Weidenhofer S, Kapsner T, et al: Skeletal muscle partial pressure of oxygen in patients with sepsis. *Crit Care Med* 1994; 22:640–650
31. Brealey D, Brand M, Hargreaves I, et al: Association between mitochondrial dysfunction and severity and outcome of septic shock. *Lancet* 2002; 360:219–223
32. Hotchkiss RS, Karl IE: The pathophysiology and treatment of sepsis. *N Engl J Med* 2003; 348:138–150
33. Sakr Y, Dubois MJ, De Backer D, et al: Persistent microcirculatory alterations are associated with organ failure and death in patients with septic shock. *Crit Care Med* 2004; 32:1825–1831
34. Trzeciak S, Dellinger RP, Parrillo JE, et al: Early microcirculatory perfusion derangements in patients with severe sepsis and septic shock: Relationship to hemodynamics, oxygen transport, and survival. *Ann Emerg Med* 2007; 49:88–98
35. De Backer D, Creteur J, Preiser JC, et al: Microvascular blood flow is altered in patients with sepsis. *Am J Respir Crit Care Med* 2002; 166:98–104
36. Bateman RM, Tokunaga C, Kareco T, et al: Myocardial hypoxia-inducible HIF-1α, VEGF, and GLUT1 gene expression is associated with microvascular and ICAM-1 heterogeneity during endotoxemia. *Am J Physiol Heart Circ Physiol* 2007; 293:H448–H456
37. Tokunaga C, Bateman RM, Boyd J, et al: Albumin resuscitation improves ventricular contractility and myocardial tissue oxygenation in rat endotoxemia. *Crit Care Med* 2007; 35:1341–1347
38. Gocan NC, Scott JA, Tyml K: Nitric oxide produced via neuronal NOS may impair vasodilatation in septic rat skeletal muscle. *Am J Physiol Heart Circ Physiol* 2000; 278: H1480–H1489
39. Scott JA, Mehta S, Duggan M, et al: Functional inhibition of constitutive nitric oxide synthase in a rat model of sepsis. *Am J Respir Crit Care Med* 2002; 165:1426–1432
40. Hollenberg SM, Broussard M, Osman J, et al: Increased microvascular reactivity and improved mortality in septic mice lacking inducible nitric oxide synthase. *Circ Res* 2000; 86:774–778
41. Yildiz G, Demiryurek AT, Sahin-Erdemli I, et al: Comparison of antioxidant activities of aminoguanidine, methylguanidine and guanidine by luminol-enhanced chemiluminescence. *Br J Pharmacol* 1998; 124:905–910
42. Bertuglia S, Giusti A: Role of nitric oxide in capillary perfusion and oxygen delivery regulation during systemic hypoxia. *Am J Physiol Heart Circ Physiol* 2005; 288:H525–H531
43. Tyml K, Li F, Wilson JX: Delayed ascorbate bolus protects against maldistribution of microvascular blood flow in septic rat skeletal muscle. *Crit Care Med* 2005; 33:1823–1828
44. Loke KE, McConnell PI, Tuzman JM, et al: Endogenous endothelial nitric oxide synthase-derived nitric oxide is a physiological regulator of myocardial oxygen consumption. *Circ Res* 1999; 84:840–845
45. Persichini T, Mazzone V, Polticelli F, et al: Mitochondrial type I nitric oxide synthase physically interacts with cytochrome c oxidase. *Neurosci Lett* 2005; 384:254–259

Research

Open Access

Fibrinogen decreases cardiomyocyte contractility through an ICAM-1-dependent mechanism

John H Boyd, Edmond H Chau, Chiho Tokunanga, Ryon M Bateman, Greg Haljan, Ehsan Y Davani, Yinjin Wang and Keith R Walley

University of British Columbia Critical Care Research Laboratories, St. Paul's Hospital, 1081 Burrard Street, Vancouver, BC, V6Z 1Y6, Canada

Corresponding author: John H Boyd, jboyd@mrl.ubc.ca

Received: 18 Jul 2007 Revisions requested: 5 Sep 2007 Revisions received: 14 Oct 2007 Accepted: 3 Jan 2008 Published: 3 Jan 2008

Critical Care 2008, 12:R2 (doi:10.1186/cc6213)

This article is online at: http://ccforum.com/content/12/1/R2

Abstract

Introduction Cardiomyocytes exposed to inflammatory processes express intracellular adhesion molecule-1 (ICAM-1). We investigated whether fibrinogen and fibrinogen degradation products, including D-dimer, could alter cardiomyocyte contractile function through interaction with ICAM-1 found on inflamed cardiomyocytes.

Methods *In vivo*, rats were injected with endotoxin to model systemic inflammation, whereas isolated rat cardiomyocytes were treated with tumor necrosis factor-alpha to model the inflammatory environment seen following exposure to bacterial products such as lipopolysaccharide.

Results *In vivo*, endotoxin administration profoundly decreased cardiac contractile function associated with a large increase in intracardiac ICAM-1 and perivascular fibrinogen. Confocal microscopy with double-staining of isolated rat cardiomyocytes demonstrated colocalization of ICAM-1 and fibrinogen. This interaction was disrupted through pre-treatment of the cells with an ICAM-1-blocking antibody. Functionally, isolated rat cardiomyocyte preparations exhibited decreased fractional shortening when incubated with fibrinogen, and through the use of synthetic peptides, we determined that residues 117–133 of the fibrinogen gamma chain are responsible for this interaction with ICAM-1. Despite having crosslinked gamma chains, D-dimer retained the ability to decrease cardiomyocyte contractility.

Conclusion Sites 117–133 of the fibrinogen gamma chain is able to depress cardiomyocyte contractility through binding ICAM-1.

Introduction

Both local and systemic inflammation impair cardiac contractility, although the precise mechanism behind this is still unclear [1-3]. It is now recognized that high levels of inflammatory biomarkers such as C-reactive protein and D-dimer are associated with an increased incidence of, and worse prognosis for, cardiovascular disease [4-8]. However, whether these molecules are simply markers of the inflammatory process or might actually play a causative role in the resultant organ dysfunction is not known. We previously reported a novel two-step regulatory mechanism of cardiomyocyte contractility whereby systemic inflammation induces cardiomyocyte-expressed intracellular adhesion molecule-1 (ICAM-1), whose subsequent ligation results in decreased contractility by signaling via the cytoskeleton [9]. While studies using cardiomyocyte/leukocyte co-culturing methods demonstrate that activated leukocytes can bind to ICAM-1 with a resultant decrease in myocardial contractility [9-11], we and others have noted a paucity of intramyocardial leukocytes in whole animal models of inflammation [12,13]. Therefore, we postulated that in the more complex environment of an *in vivo* model, ICAM-1 ligands other than the CD11/CD18 receptors found on activated leukocytes [14-16] play a greater role in ICAM-1-dependent decreases in cardiomyocyte contractility.

Fibrinogen, a 340-kDa plasma glycoprotein with a physiological plasma concentration of 1.5 to 4.5 g/L, as well as its related protein fragments D-dimer and other fibrinogen degra-

BSA = bovine serum albumin; EDV = end diastolic volume; E_{es} = end-systolic elastance; EF = ejection fraction; ELISA = enzyme-linked immunosorbent assay; E_{max} = maximal end-systolic elastance; FDP = fibrinogen degradation product; FITC = fluorescein isothiocyanate; ICAM-1 = intracellular adhesion molecule 1; Ig = immunoglobulin; LAD = left anterior descending; LPS = lipopolysaccharide; PBS = phosphate-buffered saline; TNF-α = tumor necrosis factor-alpha; vWF = von Willebrand factor; XL = crosslinking.

dation products (FDPs) represent potential ICAM-1-binding myocardial depressant substances. The amino acid sequence 117–133 of fibrinogen gamma chain (fg-γ-117–133) binds to the amino acid sequence 8–22 (ICAM-1-8–22) within the first immunoglobulin (Ig) domain of ICAM-1 [17]. The functional role of the fibrinogen-ICAM-1 interaction includes adhesion of leukocytes to endothelial cells [18,19], leukocyte transmigration [20], and promotion of endothelial cell survival [21]. Interestingly, fibrinogen-ICAM-1 ligation leads to cytoskeleton-dependent ERK1/2 (extracellular signal-regulated kinase-1/2) phosphorylation in endothelial cells [22]. In view of our previous observation in cardiomyocytes that ICAM-1 ligation by leukocytes reduces contractility via focal adhesion kinase phosphorylation at the cytoskeleton [9], fibrinogen-ICAM-1 ligation ultimately could lead to alteration in cardiomyocyte contractile function. As fragments of polymerized fibrinogen such as D-dimer are markedly elevated in most inflammatory states [4-8], it is of particular interest to determine whether these molecules are able to influence cardiac physiology through interaction with ICAM-1.

The goal of our study, therefore, was to determine whether exposure to fibrinogen and FDPs altered the contractile function of cardiomyocytes. To simulate systemic inflammation, rats were injected with endotoxin, and through immunohistochemistry, we confirmed an increase in both cardiomyocyte-expressed ICAM-1 as well as increased intramyocardial fibrinogen deposition. In isolated cardiomyocytes exposed to an inflammatory environment, we established the specificity of the fibrinogen-ICAM-1 interaction and went on to determine the active site on fibrinogen responsible for ICAM-1-mediated alterations in contractility.

Materials and methods

This study was approved by the University of British Columbia Animal Care Committee and adheres to the Canadian and National Institutes of Health guidelines for animal experimentation.

In vivo experimental models

For the endotoxin model of inflammation, male Sprague-Dawley rats 350 to 450 g in weight were injected intraperitoneally with lipopolysaccharide (LPS) (10 mg/kg) or vehicle control (normal saline). The LPS dosage was selected as a midrange dosage of endotoxemic models that result in a hemodynamic effect [23,24]. The heart was excised 6 hours after injection, embedded in Optimal Cutting Temperature compound (Electron Microscopy Sciences, Hatfield, PA, USA), frozen in dry-ice-chilled isopentane, and stored at -80°C.

Measurement of left ventricular contractility and cardiac function

Left ventricular contractility and other measures of ventricular function were determined from pressure-volume measurements using Pressure-Volume Analysis software (PVAN 2.9; Millar Instruments Inc., Houston, TX, USA). Six to ten pressure-volume loops during a vena cava occlusion were sampled and used to measure end-systolic elastance (E_{es}), which is the slope of the end-systolic pressure-volume relationship relatively insensitive to changes in preload and afterload [25]. E_{max} is defined as the maximal E_{es}. The volume axis intercept, Vd, was considered zero volume for the steady-state measurements. Pressure-volume loops measured during steady-state conditions were used to measure the maximum rate of change of intraventricular pressure during isovolumic systole divided by end diastolic volume (EDV), (dP/dt_{max})/EDV, which is a sensitive isovolumic phase measure of left ventricular contractility [26], as well as to calculate ejection fraction (EF). End-systolic pressure during steady state was used as a measure of systemic arterial pressure afterload.

Immunofluorescent imaging with quantification

Frozen heart sections (6 μm) were acetone-fixed and incubated with universal blocking agent (DakoCytomation, Glostrup, Denmark). Fibrinogen and von Willebrand factor (vWF), a marker for the endothelium, were stained together to assess whether infiltration of fibrinogen into the myocardium occurred. Sections were incubated with 1:20 fluorescein isothiocyanate (FITC)-conjugated goat anti-mouse fibrinogen (Nordic Immunological Laboratories, Tilburg, The Netherlands) and 1:200 rabbit anti-mouse vWF (DakoCytomation) primary antibody and then labeled with Alexa Fluor 594 goat anti-rabbit antibody (Invitrogen Corporation, Carlsbad, CA, USA). Nuclei were stained with the Hoechst stain (Invitrogen Corporation). Control sections were incubated with FITC-conjugated non-specific goat IgG (Santa Cruz Biotechnology, Inc., Santa Cruz, CA, USA) and non-specific rabbit IgG (DakoCytomation) and processed in identical conditions.

Immunofluorescent ICAM-1 staining was carried out by incubating sections with 1:500 mouse anti-rat ICAM-1 monoclonal antibody 1A29 (BD Biosciences, San Jose, CA, USA) and then with Alexa Fluor 594-labeled goat anti-mouse antibody (Invitrogen Corporation). Control sections were incubated with non-specific mouse IgG (Invitrogen Corporation). After drying, the slides were mounted with DABCO (1,4-diazabicyclo[2.2.2]octane) to prevent photobleaching.

Images were captured using a laser scanning confocal microscope with a 63× water immersion lens (Leica SP2; Leica, Wetzler, Germany). Samples were imaged using fluorescence with wavelength excitations and emissions of 488 nm and 495 to 580 nm (respectively) for fibrinogen and 594 nm and 600 to 700 nm (respectively) for vWF and ICAM-1. The scan format was 512 × 512 pixels. Image capturing was performed sequentially using a three-frame average. All imaging was performed under identical microscope settings (for example, laser intensity and photomultiplier tube gain).

Cross-sections of 15 randomly selected blood vessels, identified via vWF staining, were imaged. Two ellipses were traced around each vessel: a small ellipse positioned closely along the vessel boundary and a large ellipse with proportional major and minor axes but three times the area of the small ellipse. Fibrinogen staining present in the annulus between the two ellipses was identified as perivascular fibrinogen. The sum fluorescence intensity per annulus area was measured using the Leica software.

To measure myocardial ICAM-1 expression, heart sections from the endotoxemic and control groups were imaged as described above and fluorescent intensity measures were taken using traced field areas containing myocardial tissue. The sum fluorescence intensity per unit area was measured using the Leica software.

Isolation of rat ventricular myocytes

Male Sprague-Dawley rats were injected with heparin and anesthetized using isofluorane. The heart was excised, mounted on a modified Langendorff apparatus, and digested with 281 U/mL collagenase (Worthington Biochemical Corporation, Lakewood, NJ, USA). After digestion, the cells were resuspended in modified Eagle's medium containing increasing Ca^{2+} concentrations (200 μM, 500 μM, and 1 mM). Five hundred thousand cells in M199 with bovine serum albumin (BSA) were loaded into a laminin-coated Petri dish 6 cm in diameter (BD Biosciences) and the cardiomyocytes were incubated for 12 hours to allow them to become relatively quiescent. After 24 hours, cells were considered viable if they demonstrated a characteristic rod shape without cytoplasmic blebbing.

Measurement of cardiomyocyte fractional shortening

Cells were paced at 1 Hz using a Grass S48 stimulator (Grass-Telefactor, Warwick, RI, USA) with a voltage set at 120% of the threshold capture voltage. Images were captured using a Myocam video camera (IonOptix Corporation, Milton, MA, USA) and analyzed using an IonOptix Softedge detection package (IonOptix Corporation). Fractional shortening was calculated as the difference between diastolic and systolic lengths, divided by diastolic length.

Coating of fibrinogen to polystyrene beads

Polystyrene beads 8 μm in diameter (Bangs Laboratories, Inc., Fishers, IN, USA) were washed twice with acetate buffer (pH 5.4). Beads were mixed with rat fibrinogen (Enzyme Research Laboratories, South Bend, IN, USA) at a concentration of 300,000 beads per microgram of fibrinogen in a 500-μL Eppendorf tube. A micromagnetic stir bar was placed in the tube, and the mixture was gently stirred for 2 hours at room temperature. The beads were then washed three times with fresh acetate buffer. Clumps of fibrinogen-coated beads were broken apart by passing them through a syringe with a 27.5-guage needle.

ICAM-1 peptide-fibrinogen binding assay

Ninety-six-well Corning Costar 9018 enzyme-linked immunosorbent assay (ELISA) plates (eBioscience, Inc., San Diego, CA, USA) were coated for 2 hours at room temperature with fibrinogen concentrations ranging from 0.01 to 100 nM in bicarbonate/carbonate coating buffer (3.03 g of Na_2CO_3, 6.0 g of $NaHCO_3$ per 1,000 mL of distilled water) (pH 9.6). Wells were washed with phosphate-buffered saline (PBS) and then blocked overnight with 1% BSA. One hundred micromolar biotinylated ICAM-1 (8–22) sequence EAFLPRGGSVQVNCS or biotinylated scrambled peptide sequence SCNVQVSGGRPLFAE (University of British Columbia Peptide Facility, Vancouver, BC, Canada) was then added to the wells and incubated for 2 hours at room temperature before washing three times with PBS. HRP-linked anti-biotin antibody (1 μg/mL) (Invitrogen Corporation) was then added and incubated for 2 hours, followed by three washes. One hundred microliters of ABTS (2,2'-azino-di(3-ethylbenzthiazoline sulfonate) solution (Chemicon International, Temecula, CA, USA) was added to each well and incubated for 60 minutes. Absorbance values were measured at 405 nm and at 492 nm for reference.

Incubations

Twenty-four hours after cardiomyocyte isolation, cells were activated with tumor necrosis factor-alpha (TNF-α) (20 ng/mL) for 4 hours to upregulate ICAM-1 expression [9]. In studies using fibrinogen-coated beads, 25,000 beads were added to cells in laminin-coated 96-well plates (500 cells per well). A bead that moved with the contracting cardiomyocyte and maintained a contact relative location on the membrane during contraction was considered to be adherent. In studies using rat fibrinogen (Enzyme Research Laboratories), human fibrinogen, D-dimer fragments D and E (HYPHEN BioMed, Neuville-sur-Oise, France), and fibrinogen gamma chain (AnaSpec, Inc., San Jose, CA, USA) cells were incubated at concentrations of 0.03 μM, 0.1 μM, 0.3 μM, and 1 μM, respectively, for 4 hours at 37°C. After 4 hours at 37°C, cardiomyocyte fractional shortening was measured as described above.

In studies using the ICAM-1 (8–22) sequence EAFLPRGGSVQVNCS or scrambled peptide sequence SCNVQVSGGRPLFAE (University of British Columbia Peptide Facility), 1 μM rat fibrinogen and 100 μM ICAM-1 (8–22) or scrambled peptide were mixed and incubated for 4 hours at 37°C prior to incubation with cardiomyocytes as described above. In studies using anti-ICAM-1-blocking monoclonal antibody 1A29 (BD Biosciences), the antibody was added to cardiomyocytes at a concentration of 200 ng/mL 4 hours prior to the addition of fibrinogen.

Colocalization of ICAM-1 with fibrinogen

Upon TNF-α activation, cardiomyocytes were co-cultured with Oregon Green-labeled fibrinogen (Invitrogen Corporation) for 4 hours. They were then fixed with 3% paraformaldehyde for

20 minutes and blocked with universal blocking agent. Immunofluorescent ICAM-1 staining was carried out by incubating the cardiomyocytes with 1:500 mouse anti-rat ICAM-1 antibody (BD Biosciences) followed by Alexa Fluor 594-labeled goat anti-mouse antibody. The cardiomyocytes were examined using a confocal microscope (Leica) as described in the previous section. The scan format was 1,024 × 1,024 pixels, and 2× zoom was applied.

Statistical analysis

All data are expressed as mean ± standard error. For each experimental condition and time point, at least four independent replicate analyses were performed, unless otherwise noted. Differences between groups were tested using a one-way analysis of variance and the *post hoc* Bonferroni test to identify specific differences between groups. Differences were considered significant for P values of less than 0.05.

Results

Systemic inflammation depresses cardiac contractility and is associated with intracardiac extravasation of fibrinogen and increased expression of ICAM-1 by cardiomyocytes

We determined whether endotoxin would create an environment within the heart which would allow ICAM-1 expressed on cardiomyocytes to interact with extravasated fibrinogen and whether this would be associated with alterations in cardiac contractility. Six hours after LPS injection, the endotoxemic group of rats exhibited decreased left ventricular contractility compared with the saline-treated controls (Figure 1). Cardiac cycle pressure-volume loops using mean data clearly demonstrate an LPS-induced rightward shift along the volume axis. This shift reflects left ventricular dilation represented by increased EDV, maintenance of stroke volume (SV), and resultant marked reduction of left ventricular EF (EF = SV/EDV) (Figure 1 and Table 1). The preload-independent E_{max} is dramatically decreased in LPS-treated versus saline-treated rats, whereas (dP/dT)/EDV reflects isovolemic contractility and is also depressed with LPS (Table 1). Immunostaining of heart tissue from these rats demonstrated a dramatic increase in both intramyocardial ICAM-1 expression and perivascular fibrinogen in the myocardium of LPS-treated rats (Figure 2a,b). Image quantification demonstrated a 5.5 ± 1.6-fold increase in ICAM-1 expression and a 2.1 ± 0.6-fold increase in perivascular fibrinogen in the myocardium of LPS-treated rats (Figure 2c).

ICAM-1 expressed on activated isolated cardiomyocytes specifically binds to fibrinogen

By means of confocal microscopy, ICAM-1 was found to be present on the cell surface of TNF-α-activated cardiomyocytes. Co-immunostaining with fluorescently labeled fibrinogen demonstrated a high degree of colocalization (Figure 3a), supporting previous reports of interaction between these two molecules [17,21]. To confirm that fibrinogen specifically bound ICAM-1, we pre-treated isolated cardiomyocytes with either with an ICAM-1-blocking antibody or non-specific IgG. Compared with the IgG control group, cardiomyocytes treated with blocking antibody to ICAM-1 exhibited significantly lower adherence to fibrinogen-coated beads (Figure 3b). ICAM-1 is known to interact with fibrinogen via ICAM-1 peptides 8–22. To confirm this specific interaction between ICAM-1 and fibrinogen, we performed an ELISA binding assay using immobilized fibrinogen incubated with biotinylated ICAM-1 (8–22) peptide. In dose-finding experiments, as expected with receptor-ligand binding, there is a dose-response curve that reaches saturation at a fibrinogen concentration of 100 μM (Figure 4a). When group mean absorbance data are taken at this plateau fibrinogen concentration of 100 μM, there is a large increase in ICAM-1 (8–22) peptide binding with fibrinogen compared with scrambled peptide (Figure 4b). Thus, fibrinogen specifically binds to ICAM-1 through interaction with ICAM-1 peptides 8–22.

Fibrinogen mediates decreased cardiomyocyte contractility via an ICAM-1-dependent mechanism

We next examined whether ICAM-1 ligation by fibrinogen alters cardiomyocyte contractility. In one series of experiments, isolated cardiomyocytes were pre-treated with either ICAM-1-blocking antibody or isotype control antibody before adding fibrinogen-coated polystyrene beads. Whereas cardiomyocytes pre-treated with isotype control antibody demonstrated a dose-dependent decrease in contractility upon exposure to fibrinogen-coated beads, cardiomyocytes pre-treated with ICAM-1-blocking antibody demonstrated no reduction in contractility (Figure 5). To verify that this interaction is mediated

Table 1

Hemodynamic data from endotoxemic and control animals

Treatment	Heart rate (beats per minute)	Systolic pressure (mm Hg)	Ejection fraction (percentage)	(dP/dT)/EDV	E_{max}
LPS	392 ± 152	108 ± 8	38 ± 2	44 ± 3	2.5 ± 0.4
Control[a]	313 ± 30	112 ± 6	52 ± 8	121 ± 11	7.7 ± 0.6
	P = NS	P = NS	P < 0.05	P < 0.05	P < 0.05

[a]Saline-treated rats. dP, derivative of pressure; dT, derivative of time; EDV, end diastolic volume; E_{max}, maximal end-systolic elastance; LPS, lipopolysaccharide-treated rats; NS, not significant.

Figure 1

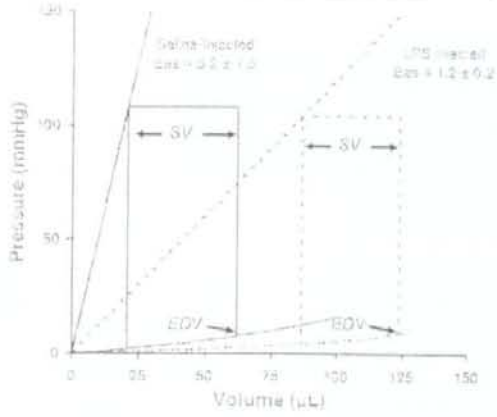

LPS decreases cardiac contractility. Cardiac cycle pressure volume loops obtained 6 hours after intraperitoneal injection of lipopolysaccharide (LPS) or saline into rats. Acquired with group mean data, the curves demonstrate an LPS-induced increased end diastolic volume (EDV), maintenance of stroke volume (SV), and therefore a marked reduction of left ventricular ejection fraction (SV/EDV). E_{es} end-systolic elastance.

specifically via the ICAM-1 (8–22) fibrinogen binding site, we performed a competitive assay in which a peptide containing the ICAM-1 (8–22) fibrinogen binding site was pre-incubated with soluble fibrinogen before addition of this mixture to activated isolated cardiomyocytes. Pre-incubation of the fibrinogen with excess ICAM-1 (8–22) peptide abolished the fibrinogen-mediated decrease in cardiomyocyte contractility, whereas pre-incubation of fibrinogen with a 'scrambled' peptide containing the same residues showed no such effect (Figure 6).

Fibrinogen chain D mediates decreased cardiomyocyte contractility

Fibrinogen is composed of three major subunits, a central E chain linked to two D chains (Figure 7a). The smaller gamma chain is always found associated with the D chain and thus is not generally considered to be a distinct subunit. To determine whether the fibrinogen-mediated contractile dysfunction results from interaction of ICAM-1 with the intact whole molecule or whether a single chain contains the binding site, cardiomyocytes were incubated with whole fibrinogen, fibrinogen chain D, or fibrinogen chain E. There was a significant decrease in cardiomyocyte contractility following incubation with whole fibrinogen and fibrinogen chain D, but no effect was seen with fibrinogen chain E (Figure 7b).

Figure 2

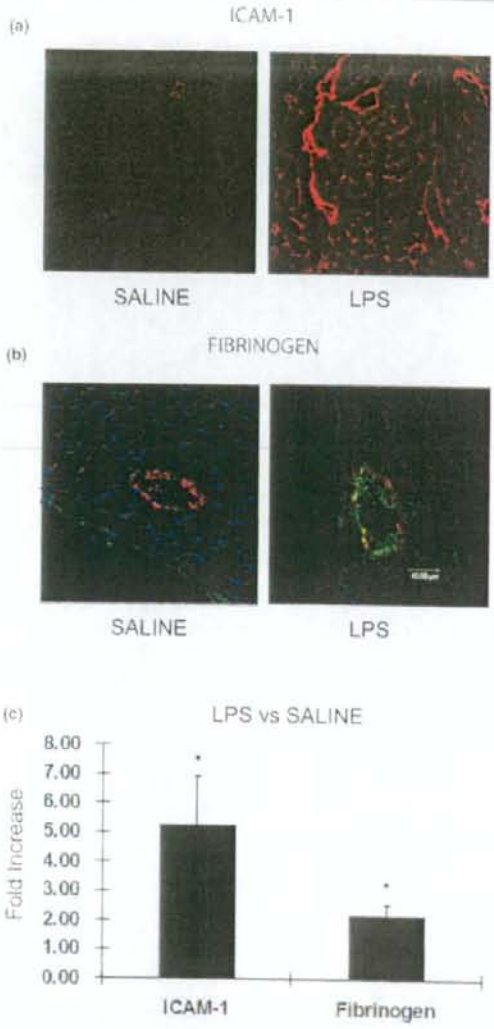

LPS increases intracardiac ICAM-1 and perivascular fibrinogen. (a) Frozen cardiac sections from lipopolysaccharide (LPS)-treated and saline-treated rats demonstrate that intracardiac intracellular adhesion molecule-1 (ICAM-1) (red) is dramatically increased in the former. (b) Fibrinogen (green) was greatly increased outside the endothelium (von Willebrand factor labeled red) in the LPS group compared with rats treated with saline. (c) Group mean data of the fold increases in myocardial ICAM-1 expression and perivascular fibrinogen deposition in LPS-treated versus saline-treated animals. *$p < 0.05$ versus saline.

Figure 3

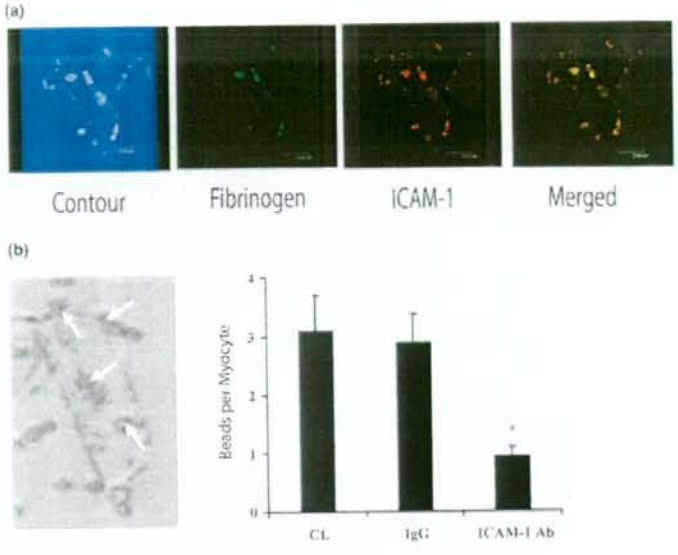

Fibrinogen binds specifically to cardiomyocyte ICAM-1. Colocalization of fibrinogen and cardiomyocyte intracellular adhesion molecule-1 (ICAM-1). **(a)** Isolated cardiomyocytes were incubated with Oregon Green-labeled fibrinogen (green) and fluorescently stained for ICAM-1 (red). A multiphoton dual-excitation image of the contour of the cell of interest is shown. By means of an overlay of images, strong colocalization of fibrinogen and ICAM-1 was indicated by a yellow color. **(b)** A representative image of a rat cardiomyocyte with adherent fibrinogen-coated polystyrene beads (white arrows) is shown to the left of the graph. The specificity of the ICAM-1-fibrinogen interaction is demonstrated as anti-ICAM-1 antibody pre-treatment results in significantly less fibrinogen-coated polystyrene beads adherent to the cardiomyocytes (*$p < 0.05$ versus control). Ab, antibody; CL, control; IgG, immunoglobulin G.

Amino acid sequence 117–133 of the fibrinogen gamma chain is the active site, and the crosslinked gamma chains of D-dimer retain the ability to interact with ICAM-1

We next determined whether the ICAM-1 binding gamma chain site 117–133 [17] of the D chain (Figure 8a) was responsible for the observed contractile dysfunction. Furthermore, as dimerization of fibrinogen chain D (commonly known as D-dimer) is accomplished in part via crosslinking the XL sites of the gamma chain (Figure 8a,b) [27], we tested whether dimerization resulted in attenuation of the ICAM-1-mediated effect. The gamma peptide 117–133 resulted in a significant reduction in fractional shortening compared with control, whereas scrambled peptide had no effect (Figure 8c). Incubation with D-dimer also resulted in a significant reduction in fractional shortening (Figure 8c), demonstrating that the functional site 117–133 remains active despite crosslinking of gamma chains.

Discussion

In this study, we propose a novel mechanism linking two phenomena that occur as a result of inflammation: dysregulation of the coagulation cascade and myocardial dysfunction. The key finding reported is that amino acid sequence 117–133 of the fibrinogen gamma chain decreases cardiomyocyte contractility through binding ICAM-1. Of great interest to clinicians is that D-dimer, a product of fibrinogen polymerization and subsequent digestion which includes 117–133 of the gamma chain, in addition to its important role in diagnosis of thromboembolism, can decrease cardiomyocyte contractility.

It has long been recognized that seemingly disparate causes of local or systemic inflammation, such as ischemia reperfusion, inflammatory cardiomyopathy, orthotopic heart transplant rejection, or sepsis [1-3], all culminate in myocardial dysfunction. While each disorder undoubtedly poses unique challenges to the maintenance of myocardial homeostasis, there could be a factor that is common to all. Endothelial damage with subsequent capillary leakage represents a final common pathway of inflammatory disorders [28]. Increased permeability of the endothelium leads to a shift of circulating elements from the plasma into the organs. Should this fluid flux contain circulating substances capable of depressing myocardial contractility, this may be the link between myocardial dysfunction and inflammatory states. This depressant not only must reach the cardiac myocytes but must have a receptor capable of mediating changes in contractility. We have previ-

Figure 4

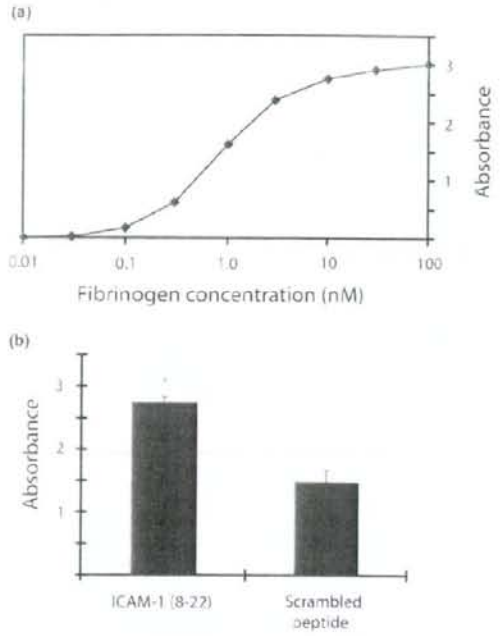

ICAM-1 (8–22) binds to fibrinogen. Two-step enzyme-linked immunosorbent assay in which fibrinogen was immobilized on the 96-well plate and then incubated with biotinylated intracellular adhesion molecule-1 (ICAM-1) (8–22) peptide or biotinylated 'scrambled' control peptide. Anti-biotin antibody was added, and colorimetric absorbance quantified the peptide-fibrinogen interaction. **(a)** Representative ICAM-1 (8–22) dose-response curve showing absorbance plateau at a fibrinogen concentration of approximately 100 μM. **(b)** Group mean absorbance data taken at the plateau fibrinogen concentration (100 μM) demonstrating a strong interaction between the ICAM-1 (8–22) peptide and fibrinogen compared with a small non-specific interaction between the scrambled peptide and fibrinogen. *$p < 0.05$ versus scrambled peptide.

ously shown that ICAM-1 expressed on cardiomyocytes is induced by inflammatory mediators and, upon activation, is capable of decreasing cardiomyocyte contractility [9,13].

Any circulating ICAM-1 ligands could be candidates for causing myocardial dysfunction provided that they permeate the heart. CD11a/CD18 (LFA-1) and Cd11b/CD18 (Mac-1) expressed on the surface of polymorphonuclear leukocytes are ICAM-1 ligands capable of reducing myocyte contractility *in vitro* [11] and have been proposed to be the link between inflammation and cardiac dysfunction. However, we and others have noted a striking paucity of intramyocardial leukocytes in whole animal models of inflammation [12,13]. Fibrinogen, as well as its related protein fragments D-dimer and other FDPs, represents potential ICAM-1 binding myocardial depressant substances. Through both human epidemiologic data and

Figure 5

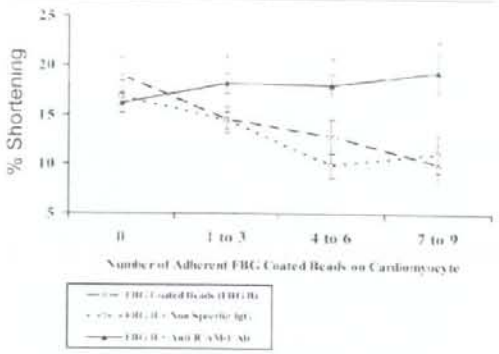

Fibrinogen decreases cardiomyocyte fractional shortening via ICAM-1. Cardiomyocytes were pre-treated with either a blocking anti-ICAM-1 antibody or isotype control antibody prior to the addition of fibrinogen-coated beads. Fractional shortening was then measured. Whereas pre-treatment with immunoglobulin G (IgG) isotype antibody was no different than fibrinogen alone, treatment with blocking anti-ICAM-1 antibody prevented the fibrinogen-induced decrease in fractional shortening. *$p < 0.05$ versus fibrinogen beads alone. Ab, antibody; FBG, fibrinogen; ICAM-1, intracellular adhesion molecule-1.

basic science, fibrinogen and FDPs satisfy two major criteria for causality. Clinically, not only are fibrinogen and D-dimer markedly increased in inflammatory disorders, but their levels are inversely correlated with favorable outcome [4-8]. As for biologic plausibility, the amino acid sequence 117–133 of fibrinogen gamma chain (fg-γ-117–133) is capable of binding the amino acid sequence 8–22 (ICAM-1-8–22) within the first Ig domain of ICAM-1 [17]. While the fibrinogen-ICAM-1 interaction facilitates adhesion of leukocytes to endothelial cells [18,19], leukocyte transmigration [20], and promotion of endothelial cell survival [21], there is no information regarding its role in cardiac physiology.

In this study, we show for the first time that fibrinogen is capable of mediating a reduction in cardiomyocyte contractility thorough activation of ICAM-1. It is important to note that significant reduction in fractional shortening was achieved at a fibrinogen concentration of 0.2 mg/mL, approximately one order of magnitude less than its physiological concentration in plasma [27]. Fibrinogen is a large 340-kDa plasma glycoprotein and, as such, would be expected to have limited tissue penetration compared with smaller plasma proteins. Despite its large size, however, we showed a significant increase in perivascular fibrinogen deposition in an *in vivo* model of systemic inflammation. FDPs, notably fragment D (100 kDa) or D-dimer at roughly double that size [27], could potentially infiltrate deeper into the myocardium and exert their depressant effect in areas that fibrinogen could not access. Importantly, not only did we find that systemic injury increased intracardiac fibrinogen, there was a dramatic increase in ICAM-1 expres-

Figure 6

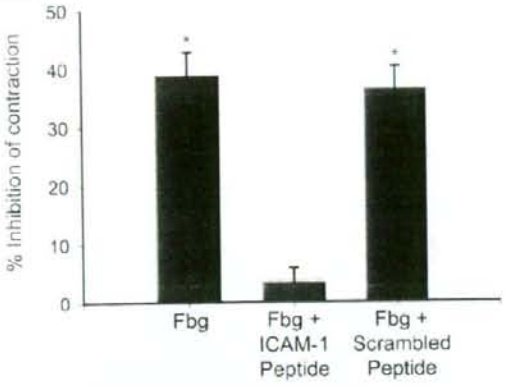

ICAM-1 (8–22) mediates decreased contractility. Before fibrinogen was added to activated cardiomyocytes, soluble intracellular adhesion molecule-1 (ICAM-1) (8–22) peptide, which binds fibrinogen at peptides 117–133, is added in excess to the fibrinogen. Activated cardiomyocytes incubated with fibrinogen alone demonstrate a 40% reduction in contractility. Pre-incubation of fibrinogen with the ICAM-1 (8–22) peptide results in competition between cardiomyocyte-expressed ICAM-1 and the ICAM-1 (8–22) peptide for the fibrinogen active site (117–133). Pre-incubation with the ICAM-1 (8–22) peptide abolishes the reduced contractility seen with fibrinogen alone, whereas pre-incubation with 'scrambled' ICAM-1 peptide had no effect. $^{*}p <$ 0.05 versus control. Fbg, fibrinogen.

Figure 7

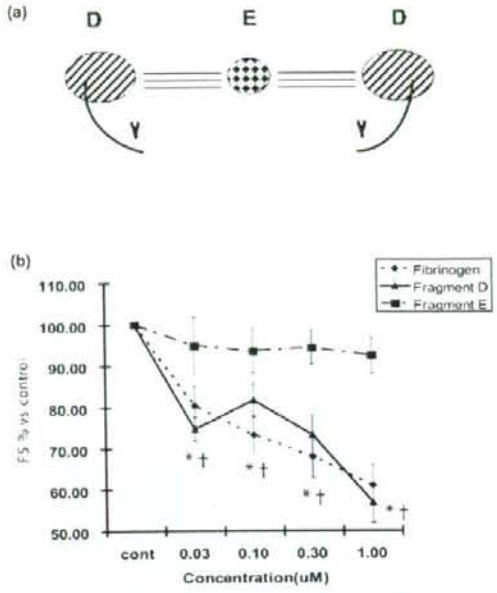

Fibrinogen subunit D decreases contractility. (a) Schematic diagram of the fibrinogen molecule, showing two D chains each containing a gamma chain linked to a central E chain. **(b)** Cardiomyocytes were incubated with whole fibrinogen as well as the major subunits D and E of fibrinogen. Whole fibrinogen and subunit D resulted in significant decreases in fractional shortening (FS), whereas subunit E had no significant effect. $^{*},^{\dagger}p < 0.05$ versus control.

sion. Thus, our animal models of disease provide *in vivo* evidence to support the hypothesis that fibrinogen and FDPs might be the circulating myocardial depressant factors.

Determining whether the previously identified interaction between fibrinogen and ICAM-1 [17-21] is responsible for alterations in cardiac physiology is fundamental information required both to understand the mechanism and to design potential therapeutics. Fibrinogen consists of two major chains, E and D, as illustrated in Figure 7a. The gamma chain is a subunit of chain D, as shown in Figures 7a and 8a, and contains a crosslinking (XL) site through which two D chains dimerize. The putative active site of fibrinogen is 117–133 on the gamma chain [17] and, though remote from the XL site as shown in Figure 8b, might be altered or allosterically interfered with upon dimerization. We show that fibrinogen chain D causes cardiomyocyte contractile dysfunction whereas chain E had no biologic effect. This agrees with findings by other investigators that it is the D chain responsible for ICAM-1-mediated vasoconstriction [29]. Furthermore, we went on to show that previously identified [17] site 117–133 of the fibrinogen gamma chain was responsible for the ICAM-1-mediated physiologic effects. As the gamma chain is linked to the D chain, it is important to consider it in the context of polymerized D chains. Despite its crosslinked gamma chains, D-dimer also caused significant reductions in contractility. Although the specificity of interaction of D-dimer with fibrinogen was not tested through antibody blockade or competing peptide, we believe that, as it is composed of two D subunits, the mechanism of action is nearly certainly analogous to the individual D chain. This last finding is particularly exciting given that, while long touted as a biomarker for both the presence and prognosis of inflammatory disease [4-8], D-dimer has been perceived, to date, as a disease marker with no intrinsic biologic effect. Not only do we now know that vascular tone can be altered by the fibrinogen D chain's activation of ICAM-1 [29], but here we demonstrate that the key contractile function of cardiac muscle cells is impaired via the same mechanism.

Conclusion

Site 117–133 of the fibrinogen gamma chain is able to depress cardiomyocyte contractility through binding ICAM-1. The implication of the reported mechanism extends beyond the realm of our models of inflammation to other pathologies characterized by inflammation and heart failure, such as post-ischemia reperfusion injury, inflammatory cardiomyopathy, and orthotopic heart transplant rejection.

Figure 8

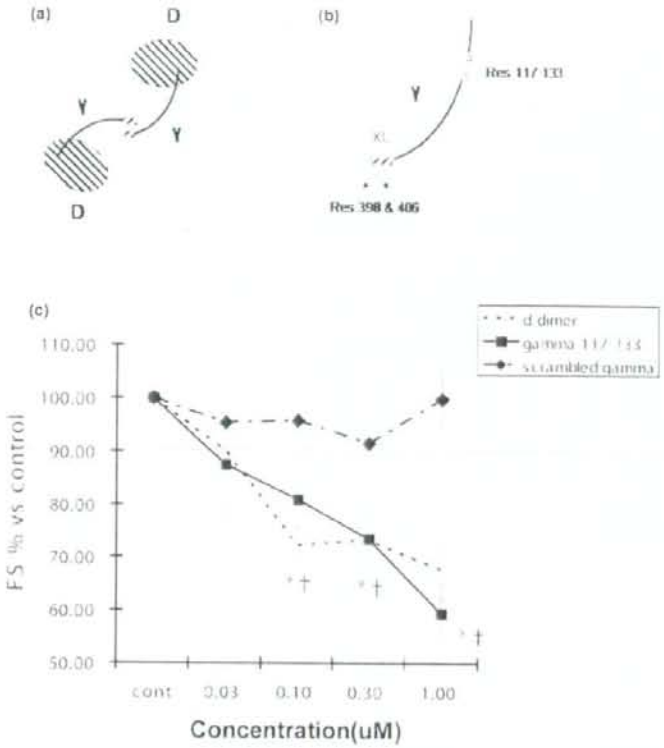

Fibrinogen gamma chain and D-dimer decrease contractility. **(a)** Schematic diagram of D-dimer with two D subunits linked in part via interaction of the gamma chains. For simplicity, we have not shown the areas on the D chain itself which participate in dimerization. **(b)** Expanded diagram of the gamma subunit showing the crosslinking (XL) site of the C-terminal regions which results in amine donor lysine 406 of one gamma chain and a glutamine acceptor at residue 398 or 399. The intracellular adhesion molecule-1 (ICAM-1) binding site is shown as residue 117–133, far removed from the XL site. **(c)** Cardiomyocytes were incubated with a peptide with the sequence 117–133, D-dimer, or scrambled peptide. D-dimer and the gamma (117–133) peptide resulted in significant decreases in fractional shortening (FS), whereas scrambled peptide had no significant effect. *,†$p < 0.05$ versus control.

Key messages

- Intracardiac intracellular adhesion molecule-1 (ICAM-1) and fibrinogen are increased as a result of systemic inflammation.
- Amino acid sequence 117–133 of the fibrinogen gamma chain is responsible for binding ICAM-1, functionally decreasing cardiomyocyte contractility.
- D-dimer contains the fibrinogen gamma chain and also decreases cardiomyocyte contractility.

Competing interests

The authors declare that they have no competing interests.

Authors' contributions

JHB drafted the manuscript. EHC performed the initial contractility measurements. EYD helped design the contractility experiments. CT performed the peptide experiments. RMB performed immunohistochemistry. GH designed the peptides. YW performed the animal work. KRW conceived of the study, participated in its design and coordination, and helped to draft the manuscript. All authors read and approved the final manuscript.

Acknowledgements

This work was supported by the Canadian Institutes of Health Research. KRW is a Michael Smith Foundation for Health Research (MSFHR) Distinguished Scholar. JHB is an IMPACT (Integrated and mentored pulmonary and cardiovascular training) postdoctoral fellow. RMB is an MSFHR postdoctoral fellow.

References

1. Van Eyk JE, Powers F, Law W, Larue C, Hodges RS, Solaro RJ: **Breakdown and release of myofilament proteins during ischemia and ischemia/reperfusion in rat hearts: identification of degradation products and effects on the pCa-force relation.** *Circ Res* 1998, **82**:261-271.
2. Reilly JM, Cunnion RE, Burch-Whitman C, Parker MM, Shelhamer JH, Parrillo JE: **A circulating myocardial depressant substance is associated with cardiac dysfunction and peripheral hypoperfusion (lactic acidemia) in patients with septic shock.** *Chest* 1989, **95**:1072-1080.
3. Yano M, Ono K, Ohkusa T, Suetsugu M, Kohno M, Hisaoka T, Kobayashi S, Hisamatsu Y, Yamamoto T, Noguchi N, *et al.*: **Altered stoichiometry of FKBP12.6 versus ryanodine receptor as a cause of abnormal Ca(2+) leak through ryanodine receptor in heart failure.** *Circulation* 2000, **102**:2131-2136.
4. Lowe GD, Rumley A, McMahon AD, Ford I, O'Reilly DS, Packard CJ: **Interleukin-6, fibrin D-dimer, and coagulation factors VII and XIIa in prediction of coronary heart disease.** *Arterioscler Thromb Vasc Biol* 2004, **24**:1529-1534.
5. Lowe GD: **Circulating inflammatory markers and risks of cardiovascular and non-cardiovascular disease.** *J Thromb Haemost* 2005, **3**:1618-1627.
6. McDermott MM, Ferrucci L, Liu K, Criqui MH, Greenland P, Green D, Guralnik JM, Ridker PM, Taylor LM, Rifai N, *et al.*: **D-dimer and inflammatory markers as predictors of functional decline in men and women with and without peripheral arterial disease.** *J Am Geriatr Soc* 2005, **53**:1688-1696.
7. Heuer JG, Sharma GR, Gerlitz B, Zhang T, Bailey DL, Ding C, Berg DT, Perkins D, Stephens EJ, Holmes KC, *et al.*: **Evaluation of protein C and other biomarkers as predictors of mortality in a rat cecal ligation and puncture model of sepsis.** *Crit Care Med* 2004, **32**:1570-1578.
8. Sagastagoitia JD, Sáez Y, Vacas M, Narváez I, Sáez de Lafuente JP, Molinero E, Magro A, Lafita M, Santos M, Escobar A, *et al.*: **Association between inflammation, lipid and hemostatic factors in patients with stable angina.** *Thromb Res* 2007, **120**:53-59.
9. Davani EY, Dorscheid DR, Lee CH, van Breemen C, Walley KR: **Novel regulatory mechanism of cardiomyocyte contractility involving ICAM-1 and the cytoskeleton.** *Am J Physiol Heart Circ Physiol* 2004, **287**:H1013-1022.
10. Poon BY, Ward CA, Cooper CB, Giles WR, Burns AR, Kubes P: **Alpha(4)-integrin mediates neutrophil-induced free radical injury to cardiac myocytes.** *J Cell Biol* 2001, **152**:857-866.
11. Entman ML, Youker K, Shoji T, Kukielka G, Shappell SB, Taylor AA, Smith CW: **Neutrophil induced oxidative injury of cardiac myocytes. A compartmented system requiring CD11b/CD18-ICAM-1 adherence.** *J Clin Invest* 1992, **90**:1335-1345.
12. Raeburn CD, Calkins CM, Zimmerman MA, Song Y, Ao L, Banerjee A, Harken AH, Meng X: **ICAM-1 and VCAM-1 mediate endotoxemic myocardial dysfunction independent of neutrophil accumulation.** *Am J Physiol Regul Integr Comp Physiol* 2002, **283**:R477-486.
13. Davani EY, Boyd JH, Dorscheid DR, Wang Y, Meredith A, Chau E, Singhera GK, Walley KR: **Cardiac ICAM-1 mediates leukocyte-dependent decreased ventricular contractility in endotoxemic mice.** *Cardiovasc Res* 2006, **72**:134-142.
14. Landis RC, McDowall A, Holness CL, Littler AJ, Simmons DL, Hogg N: **Involvement of the "I" domain of LFA-1 in selective binding to ligands ICAM-1 and ICAM-3.** *J Cell Biol* 1994, **126**:529-537.
15. Staunton DE, Marlin SD, Stratowa C, Dustin ML, Springer TA: **Primary structure of ICAM-1 demonstrates interaction between members of the immunoglobulin and integrin supergene families.** *Cell* 1988, **52**:925-933.
16. Clayton A, Evans RA, Pettit E, Hallett M, Williams JD, Steadman R: **Cellular activation through the ligation of intercellular adhesion molecule-1.** *J Cell Sci* 1998, **111 (Pt 4)**:443-453.
17. Duperray A, Languino LR, Plescia J, McDowall A, Hogg N, Craig AG, Berendt AR, Altieri DC: **Molecular identification of a novel fibrinogen binding site on the first domain of ICAM-1 regulating leukocyte-endothelium bridging.** *J Biol Chem* 1997, **272**:435-441.
18. Languino LR, Plescia J, Duperray A, Brian AA, Plow EF, Geltosky JE, Altieri DC: **Fibrinogen mediates leukocyte adhesion to vascular endothelium through an ICAM-1-dependent pathway.** *Cell* 1993, **73**:1423-1434.
19. Languino LR, Duperray A, Joganic KJ, Fornaro M, Thornton GB, Altieri DC: **Regulation of leukocyte-endothelium interaction and leukocyte transendothelial migration by intercellular adhesion molecule 1-fibrinogen recognition.** *Proc Natl Acad Sci USA* 1995, **92**:1505-1509.
20. Sans E, Delachanal E, Duperray A: **Analysis of the roles of ICAM-1 in neutrophil transmigration using a reconstituted mammalian cell expression model: implication of ICAM-1 cytoplasmic domain and Rho-dependent signaling pathway.** *J Immunol* 2001, **166**:544-551.
21. Gardiner EE, D'Souza SE: **Sequences within fibrinogen and intercellular adhesion molecule-1 (ICAM-1) modulate signals required for mitogenesis.** *J Biol Chem* 1999, **274**:11930-11936.
22. Pluskota E, D'Souza SE: **Fibrinogen interactions with ICAM-1 (CD54) regulate endothelial cell survival.** *Eur J Biochem* 2000, **267**:4693-4704.
23. Parker JL: **Contractile function of heart muscle isolated from endotoxin-shocked guinea pigs and rats.** *Adv Shock Res* 1983, **9**:133-145.
24. Heneka MT, Loschmann PA, Osswald H: **Polymerized hemoglobin restores cardiovascular and kidney function in endotoxin-induced shock in the rat.** *J Clin Invest* 1997, **99**:47-54.
25. Nozawa T, Yasumura Y, Futaki S, Tanaka N, Uenishi M, Suga H: **Efficiency of energy transfer from pressure-volume area to external mechanical work increases with contractile state and decreases with afterload in the left ventricle of the anesthetized closed-chest dog.** *Circulation* 1988, **77**:1116-1124.
26. Kass DA, Maughan WL, Guo ZM, Kono A, Sunagawa K, Sagawa K: **Comparative influence of load versus inotropic states on indexes of ventricular contractility: experimental and theoretical analysis based on pressure-volume relationships.** *Circulation* 1987, **76**:1422-1436.
27. Walker JB, Nesheim ME: **The molecular weights, mass distribution, chain composition, and structure of soluble fibrin degradation products released from a fibrin clot perfused with plasmin.** *J Biol Chem* 1999, **274**:5201-5212.
28. Lindbom L: **Regulation of vascular permeability by neutrophils in acute inflammation.** *Chem Immunol Allergy* 2003, **83**:146-166.
29. Lominadze D, Tsakadze N, Sen U, Falcone JC, D'Souza SE: **Fibrinogen and fragment D-induced vascular constriction.** *Am J Physiol Heart Circ Physiol* 2005, **288**:H1257-1264.

hypertension, and attenuated the histological appearance of the lung damage, without an obvious protective effect on organ function and respiratory mechanics.

References

1. Otterbein L, *et al.*: *Nat Med* 2000, **6**:422-428.
2. Hoetzel A, *et al.*: *Antioxid Redox Signal* 2007, **9**:2013-2026.

P395

Endotoxemia induces an early differential metabolic response in the heart and liver as determined by metabolomic analysis

RM Bateman, M Ohmura, Y Nagahata, T Hishiki, M Suematsu
Keio University, Tokyo, Japan
Critical Care 2008, **12(Suppl 2)**:P395 (doi: 10.1186/cc6616)

Introduction Sepsis induces a hypermetabolic state and impairs energy metabolism. In this preliminary small animal study, we used recently developed metabolomics technology to test the hypothesis that metabolic shifts in glucose and amino acid metabolism in the heart and liver occur during the onset of endotoxemia.

Methods Sepsis was modeled in C57BL/6 mice via administration of lipopolysaccharide (LPS) (intraperitoneally, 40 mg/kg). Five hours post LPS, the left lobe of the liver and the heart were harvested. High-throughput capillary electrophoresis–mass spectrometry was used to identify and quantify metabolite levels based on their unique mass/charge ratio. The advantage of this metabolomics approach is that over 1,000 charged species can be detected in a single sample, generating a unique metabolic profile or readout.

Results Figure 1 shows relative changes in glucose and glycolytic metabolites, Kreb's cycle intermediates, NADH, ATP and amino acids between 5-hour LPS ($n = 2$) and control mice ($n = 2$). Metabolomic analysis suggested that endotoxemia caused an early increase in glucose metabolism in the heart, but a decrease in the liver. NADH levels increased in the liver, but not the heart, while ATP levels decreased in both the liver and the heart. Amino acid levels increased in the liver, with the exception of alanine and glycine, but were more variable in the heart.

Conclusions Five hours after LPS administration, we found differential glucose and amino acid metabolism in the heart and liver, indicating that profound shifts in metabolism occurred during the onset of endotoxemia.

P396

Noradrenaline for treatment of endotoxemic shock in pigs is associated with improved hepatic mitochondrial respiration

T Regueira, S Djafarzadeh, PM Lepper, B Bänziger, S Brandt, J Takala, SM Jakob
Bern University Hospital (Inselspital), University of Bern, Switzerland
Critical Care 2008, **12(Suppl 2)**:P396 (doi: 10.1186/cc6617)

Introduction The optimal mean arterial blood pressure (MAP) for sepsis resuscitation remains unclear. Growing evidence suggests that mitochondrial dysfunction plays a role in the pathogenesis of sepsis-induced organ failures. The aim of this study was to evaluate the effect of progressively increasing levels of MAP, achieved by the use of noradrenaline (NA) on liver mitochondrial function during sepsis.

Methods Thirteen anesthetized pigs received endotoxin (*Escherichia coli* LPS B0111:B4, 0.4 μg/kg/hour until the mean pulmonary arterial pressure reached 35 mmHg) and were subsequently randomized to placebo or NA administration for 10 hours. The NA dose was adjusted every 2 hours to achieve 15 mmHg increases in MAP up to 95 mmHg. Systemic (thermodilution) and hepatosplanchnic blood flow (ultrasound Doppler) were measured at each step. At the end of the experiment, hepatic mitochondrial oxygen consumption (high-resolution respirometry) and citrate synthase activity (spectrophotometrically) were assessed, using the Oxygraph 2K (Oroboros Instruments, Innsbruck, Austria) and DatLab 4.2 software for data acquisition and analysis.

Results The MAP, cardiac output and systemic DO_2 increased in the NA group to 95 ± 7 mmHg (controls: 64 ± 3 mmHg), 8.7 ± 3.1 l/min (controls: 5.7 ± 1.4 l/min), and 33 ± 8 ml/min/kg (controls: 17.6 ± 3.4 ml/min/kg; all $P < 0.05$). Systemic and hepatosplanchnic VO_2 were not different between groups. Hepatic lactate uptake decreased significantly in both groups, but without differences between the groups. At the end of the experiment, liver mitochondrial function in the NA group exhibited a significant improvement in terms of maximal complex I-dependent mitochondrial respiration (from 329 ± 83 to 587 ± 195 pmol/s/mg), and of respiratory control ratio for complex I (from 3.8 ± 1.3 to 5.7 ± 0.5) and complex II (from 3.2 ± 0.5 to 3.9 ± 0.6; all $P < 0.05$). There were no differences in citrate synthase activity between the groups (13.9 ± 3 vs 16.8 ± 4 μmol/min/mg).

Figure 1 (abstract P395)

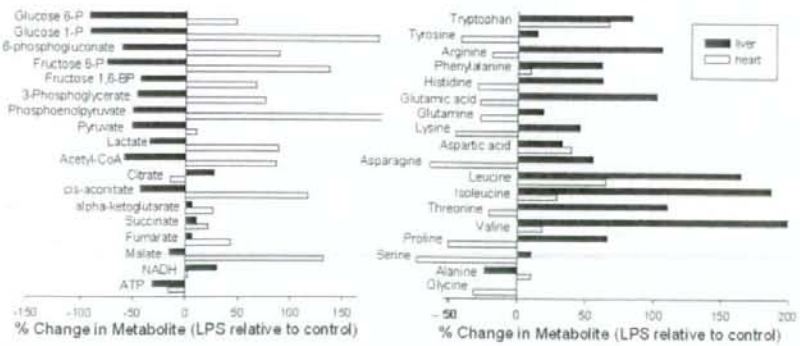

Metabolic profiles for glucose (left) and amino acid (right) metabolism.

Endotoxemia induces a differential metabolic response in the heart and liver as determined by metabolomic analysis

Ryon M Bateman[1], Reiichiro Obata[1], Yoshiko Nagahata[1], Mitsuyo Ohmura[1], Takako Hishiki[1], Makoto Suematsu[1]. Department of Biochemistry and Integrative Medical Biology, School of Medicine, Keio University, 160-8582, Tokyo, Japan

(characters 339/400)

The systemic inflammatory response to bacterial infection (sepsis) alters microvascular and mitochondrial function; yet, little is known about effects on metabolism. The objective was to determine how intermediary carbohydrate metabolism changes during the onset of sepsis. C57bl/6 mice (30-35g) were injected intraperitoneally with lipopolysaccharide (LPS, 40mg/kg). Six hours post LPS, C13-pyruvate (a key intermediate metabolite) was administered subcutaneously. At 20,40 and 60 minutes, heart and liver tissues were harvested and stored at -80C. Capillary electrophoresis - mass spectrometry (CE-MS) quantified metabolic intermediates. Labeled metabolites were normalized to non-labeled metabolite levels. Pyruvate was preferentially metabolized by the heart, but uptake was delayed in both liver and heart relative to control. Lactate, TCA intermediates (citrate, a-ketoglutarate, malate), G1P and UDP-glucose increased in the endotoxemic heart. By contrast, glutamate and B-hydroxybutyrate increased in endotoxemic liver. Fluxome analysis of pyruvate metabolism suggests the endotoxemic heart stores glucose, while the liver generates alternative energy sources. Funding source, MEXT Japan.

 Articles in PresS. Am J Physiol Renal Physiol (October 29, 2008). doi:10.1152/ajprenal.00013.2008

CD36 is one of important receptors promoting renal tubular injury by advanced oxidation protein products

Yasunori Iwao[1], Keisuke Nakajou[1], Ryoji Nagai[2], Kenichiro Kitamura[3], Makoto Anraku[1], Toru Maruyama[1], Masaki Otagiri[1*]

[1]Department of Biopharmaceutics, Graduate School of Pharmaceutical Sciences, Kumamoto University, Kumamoto, Japan

[2] Department of Medical Biochemistry, Graduate School of Medical Sciences, Kumamoto University, Kumamoto, Japan

[3] Department of Nephrology, Graduate School of Medical Sciences, Kumamoto University, Kumamoto, Japan

Running head:

CD36 is involved in renal tubular injury caused by AOPPs

*Address correspondence to:

Masaki Otagiri, Ph.D.

Professor

Department of Biopharmaceutics,

Graduate School of Pharmaceutical Sciences,

Kumamoto University

5-1 Oe-honmachi, Kumamoto 862-0973, Japan

Phone: +81-96-371-4150

Fax: +81-96-362-7690

E-mail: otagirim@gpo.kumamoto-u.ac.jp